Published in final edited form as:
J Magn Reson Imaging. 2008 February ; 27(2): 376–390. doi:10.1002/jmri.21265.

MR Thermometry

Viola Rieke, PhD* and **Kim Butts Pauly, PhD**
Department of Radiology, Stanford University, Stanford, California

Abstract

Minimally invasive thermal therapy as local treatment of benign and malignant diseases has received increasing interest in recent years. Safety and efficacy of the treatment require accurate temperature measurement throughout the thermal procedure. Noninvasive temperature monitoring is feasible with magnetic resonance (MR) imaging based on temperature sensitive MR parameters such as the proton resonance frequency (PRF), the diffusion coefficient (D), T_1 and T_2 relaxation times, magnetization transfer, the proton density, as well as temperature sensitive contrast agents. In this paper, the principles of temperature measurements with these methods will be reviewed and their usefulness for monitoring in vivo procedures will be discussed. Whereas most measurements give a temperature change relative to a baseline condition, temperature sensitive contrast agents and spectroscopic imaging can provide absolute temperature measurements. The excellent linearity and temperature dependence of the PRF and its near independence of tissue type have made PRF based phase mapping methods the preferred choice for many in vivo applications. Accelerated MRI imaging techniques for real-time monitoring with the PRF method will be discussed. Special attention is paid to acquisition and reconstruction methods for reducing temperature measurement artifacts introduced by tissue motion, which is often unavoidable during in vivo applications.

Keywords

thermometry; temperature; thermal therapy; diffusion; relaxation; proton resonance frequency shift; PRF; fat; motion artifacts

INTRODUCTION

Minimally invasive thermal therapy of benign and malignant diseases benefits from near real-time MR image guidance. In part, this is due to the attractive properties of MRI, such as its non-invasiveness, lack of ionizing radiation, and the ability to image in any scan orientation with good spatial and temporal resolution. However, it is the ability of MRI to construct maps of in vivo body temperature that make it particularly well suited for guiding and monitoring minimally invasive thermal therapy.

Thermal therapy can be divided into two regimes. The first is low-temperature hyperthermia, where temperatures in the range of 43–45°C are applied for a time of several tens of minutes to kill cancer cells directly or to sensitize them to cytotoxic agents and/or radiation (1). The second is high-temperature thermal ablation, where temperatures in the range of 50–80°C (or higher) are applied for a shorter amount of time to rapidly coagulate the tissue and induce necrosis through processes such as protein denaturation (2).

*Correspondence to: Viola Rieke, Department of Radiology, Lucas MRI Center, 1201 Welch Road, Stanford, CA 94305-5488. Phone: (650) 724-9574, Fax: (650) 723-5795, vrieke@stanford.edu.

The goal of MR image-guided thermal therapy is to use real-time temperature mapping to provide more control over the treatment outcome. Therefore, it is not only necessary to accurately measure the temperature during treatment, but also to be able to relate treatment temperature to actual thermal tissue damage. A model that is widely used in thermal therapy is the *thermal dose* model (3). Based on the Arrhenius-damage integral, this model quantifies damage using temperature and time in a non-linear fashion and relates it to an equivalent heating time at 43°C. The thermal dose required for total necrosis ranges from 25 to 240 min at 43°C for biological tissues (4). Figure 1 shows the maximum temperature and thermal dose map in comparison to a contrast-enhanced post-treatment image from in vivo ultrasound ablation in a canine prostate.

Different methods to apply energy in thermal therapies have been investigated and are used in clinical practice. Laser-induced interstitial thermotherapy (LITT) is a minimally invasive treatment that uses a laser fiber with a diffusing tip to deposit energy into the tissue. Because there is no interference of the laser with the MR scanner, LITT is well suited for image-based thermal monitoring. Lesion sizes achieved with the laser are relatively small, but catheter cooled systems (5) are available that achieve larger lesion sizes.

Ultrasound is another method for energy deposition into tissue. Focused ultrasound (FUS), also referred to as high intensity focused ultrasound (HIFU), is a completely non-invasive method that uses an external transducer to focus the ultrasound beam from outside the patient without an incision (6). Moving the focus of the beam through the tissue allows ablation of irregular shaped regions. Interstitial, transurethral (7) and transrectal ultrasound use MRI compatible, multi-element ultrasound transducers and provide spatial control over the heating area.

For radiofrequency (RF) ablation, an interstitial electrode which delivers alternating current is placed into the tissue. Some electrodes have a number of tines at their tip that are deployed to increase the ablation zone. During RF-ablation, tissue temperature in the space around the electrode increases by ohmic heating. Because MR systems are highly susceptible to interference from the RF ablation device, appropriate filtering has to be implemented (8) or ablation and MR data acquisition need to be interleaved (9,10).

Microwave heating for thermal ablation uses a small interstitial microwave antenna operated at a frequency between 1–3 GHz (11). For microwave ablation, several antennas can be used simultaneously to create large lesions sizes.

These thermal therapy methods have a common goal: selective tumor treatment that does not damage healthy tissue. During thermal therapy it has to be ensured that the entire diseased tissue volume has been exposed to an adequate temperature over a specific time to induce necrosis while avoiding the destruction of surrounding healthy tissue (3). Several factors make predicting the heating distribution difficult. Because energy deposition at the target depends on the tissue's ability to absorb the applied energy, it is a function of tissue composition. The tissue parameters can change as the tissue undergoes changes during thermal treatment, for example when proteins coagulate. In addition, heat conduction through perfusion and diffusion can vary with tissue architecture, tissue composition and physiological parameters, such as during a temperature-dependent increase in perfusion.

Therefore, the role of MRI is to visualize and quantify the deposition of heat energy in the treated and surrounding tissue with adequate spatial and temporal resolution. Consequently, the success of MR image-guided thermal therapy depends on the accuracy with which temperature can be estimated. In this paper, the different methods for MR temperature mapping are reviewed and compared with respect to temperature sensitivity, linearity of temperature effects, acquisition speed, potential artifacts and motion sensitivity. Methods that are frequently

used to monitor temperature during interventional procedures are covered in more detail, and less common methods are treated briefly for completeness. In 2000, Quesson *et al*. (12) gave an excellent review on MR thermometry methods in this journal. Although there is some overlap in the principles of the temperature methods in this review, the focus is on new developments since then.

OVERVIEW OF MRI TEMPERATURE METHODS

A number of MR parameters show a sensitivity to temperature: the proton density, the T_1 and T_2 relaxation times, the diffusion coefficient, magnetization transfer, and the proton resonance frequency (PRF). In addition to these intrinsic parameters, temperature-sensitive contrast agents have been developed. Depending on the technique, the temperature measurement is absolute (e.g. in spectroscopy) or gives a relative temperature change by comparing the acquired data to reference data, acquired under identical experimental conditions at a known temperature.

Proton Density

The proton density depends linearly on the equilibrium magnetization M_0, which is determined by the Boltzmann distribution (13):

$$PD \propto M_0 = \frac{N\gamma^2\hbar^2 I(I+1)B_0}{3\mu_0 kT} = \chi_0 B_0, \quad (1)$$

where N is the number of spins per volume, γ is the gyromagnetic ratio, h_{bar} is Planck's constant, I is the quantum number of the spin system (1/2 for protons), B_0 is the magnetic flux density, μ_0 is the permeability of free space, k is the Boltzmann constant, T is the absolute temperature of the sample, and χ_0 is the susceptibility. The relationship of χ_0 and temperature is known as the Curie law:

$$\chi_0 \propto \frac{1}{T} \quad (2)$$

Because M_0 depends on the Boltzmann thermal equilibrium, it is possible to evaluate temperature changes based on proton density weighted images. Please note, that the proton density in the tissue itself does not change with temperature but rather the susceptibility which reflects the ratio of parallel and anti-parallel spin populations. The temperature sensitivity of M_0 is inversely proportional to temperature and changes by −0.30 ± 0.01%/°C (14) between 37°C and 80°C. From the change in proton density a relative temperature is calculated. However, the temperature dependency −0.3%/°C is small, requiring high signal-to-noise ratio (SNR), e.g. an SNR of 100 is required for a temperature uncertainty of 3°C (15). To eliminate effects from changes in T_1 relaxation time, long repetition times close to 10 s are required, making the method less useful for real-time applications. In fast imaging sequences changes in proton density are difficult to separate from effects due to changes in relaxation times (16). This method has been used to measure temperature changes in ex vivo tissue samples, including fat (15).

T_1 Relaxation Time of Water Protons

The temperature dependence of the T_1 relaxation time was first shown by Bloembergen *et al*. (17) and subsequently investigated by Parker (18) for non-invasive thermometry in MRI. Spin-lattice relaxation in biologic tissues results from dipolar interactions of macromolecules and

water molecules, which arise from their translational and rotational motion. The temperature dependence of this motion is reflected in changes to the spin-lattice relaxation time T_1 (13), which increases with an increase in temperature. One model that describes the variation of the T_1 relaxation time of water protons is (19):

$$T_1 \propto e^{-E_a(T_1)/kT}, \tag{3}$$

where $E_a(T_1)$ is the activation energy of the relaxation process, k is the Boltzmann constant, and T is the absolute temperature. More information on the derivation of the temperature dependence of the relaxation times can be found in Bottomley et al. (20). Within a small temperature range T_1 depends linearly on temperature, but both T_1 and its temperature dependence are different for different tissues. The temperature dependence of the longitudinal relaxation times can be described as

$$T_1(T)=T_1(T_{\text{ref}})+m\cdot(T-T_{\text{ref}}), \tag{4}$$

where $m = dT_1/dT$ is determined empirically for each tissue (21), and T_{ref} is the reference temperature. Temperature dependence was found to be in the order of 1%/°C (22), with values of 1.4%/°C in bovine muscle (23), 1–2%/°C in liver (24), and 0.97%/°C in fat (25).

The signal for both spin echo or gradient echo images can be expressed in terms of M_0, the flip angle α, the relaxation time T_1 and the repetition time TR as

$$S=M_0 sin\alpha\frac{1-E_1}{1-cos\alpha E_1}, \tag{5}$$

where

$$E_1=exp\left[-\frac{TR}{T_1(T_{\text{ref}})+m(T-T_{\text{ref}})}\right]. \tag{6}$$

The relative temperature sensitivity of the magnitude image dS/SdT is related to the rate of signal change with relaxation dS/dT_1

$$\frac{dS}{dT}=m\cdot\frac{dS}{dT_1} \tag{7}$$

Note, that both M_0 and T_1 change with temperature. The signal decreases with increasing temperature both because the relaxation time increases and the magnetization decreases. The small nonlinear temperature dependence on the equilibrium magnetization is often neglected (26) or, alternatively, Eq. 7 is modified to (27)

$$\frac{dS}{dT}=m\cdot\frac{dS}{dT_1}-\frac{S}{T}, \tag{8}$$

where the second term on the right hand side represents the decrease in the equilibrium magnetization with increasing absolute temperature, as given by Eq. 1. The spin-spin relaxation time T_2 is also a function of temperature. The temperature dependence, however, is relatively small (28) and usually neglected. Using Eqs. 5 and 8, the temperature sensitivity dS/SdT is then given by:

$$\frac{dS}{SdT} = -\frac{mTR(1-cos\alpha)E_1}{T_1(T_{ref})^2(1-E_1)(1-cos\alpha E_1)} - \frac{1}{T_{ref}}. \quad (9)$$

The quality of T_1-based thermal mapping depends on the accuracy of measuring and extracting T_1. Many accurate T_1 mapping methods such as inversion recovery and saturation recovery are very time consuming and not useful for monitoring thermal therapy, although single-shot methods partially alleviate the problem. A fast T_1 mapping method, T_1 by multiple read-out pulses (TOMROP), allows acquisition of multiple slices in about four minutes, which might be an acceptable time frame for hyperthermia (29). Lipid suppression should be used, because the presence of lipids, which have a different T_1 change with temperature, is a potential source of artifacts. In addition, a temperature gradient within a single voxel can cause phase dispersion due to PRF changes that may decrease the received signal independent from T_1-changes. Using spin-echo methods, which refocus the phase dispersion, eliminates this problem.

The quantification of temperature changes using T_1 effects is difficult because the temperature coefficient of the individual tissues is usually not known and the physiologic response of the living tissue to heat can seriously affect the quantification (30). Nonlinear effects can also occur if the tissue properties change, e.g. due to coagulation, which has been found in ex vivo tissue to occur at temperatures as low as 43°C (29). Because of these problems, T_1 changes are often only used to get a qualitative measure of the temperature distribution. If only a qualitative temperature measurement is needed, T_1-weighted images can be acquired rapidly and compared to or subtracted from baseline images acquired before heating. Figure 2 gives an example of the signal decrease during RF-heating in a T_1-weighted gradient echo image.

T_1 and the T_1-change per °C (20) increase with increasing field strength, but T_1 contrast diminishes (30). Thus, apart from SNR advantages at higher field, T_1-based temperature mapping using T_1-weighted images appears more sensitive at low field (12). T_1-weighted images can be acquired with relatively motion-insensitive pulse sequences, but image registration between successive images has to be ensured. Figure 3 shows an example of a T_1-weighted thermosensitive gradient echo images to monitor laser-induced interstitial thermotherapy (LITT) (31).

T_2 Relaxation Time of Water Protons

A similar increase in T_2 relaxation time with increasing temperature has been observed in aqueous solutions. In tissue however, water T_2 is reduced by a significant factor compared to pure water and the temperature dependence of T_2 can be masked by other factors. Observing a T_2-weighted MR signal in tissue over temperature, the signal undergoes a pronounced decrease at higher temperatures (33) and remains at the lower signal level during cooling to room temperature. This change in T2 relaxation could be a defining characteristic of irreversible tissue damage due to thermal coagulation. The measured T_2-change with temperature is therefore nonlinear but shows a sigmoidal increase (33). Temperature measurements in adipose tissue have also been demonstrated (34).

Diffusion - Brownian Molecular Motion

This method is based on the temperature dependence of the diffusion coefficient D which describes the thermal Brownian motion of an ensemble of molecules in a medium. The relationship between temperature and diffusion coefficient can be written as (35):

$$D \approx e^{-E_a(D)/kT}, \tag{10}$$

where $E_a(D)$ is the activation energy of the molecular diffusion of water, k is the Boltzmann constant, and T is absolute temperature. The temperature dependence is described by:

$$\frac{dD}{DdT} = \frac{E_a(D)}{kT^2} \tag{11}$$

with a temperature sensitivity of about 2%/°C.

Random Brownian motion of molecules results in a Gaussian distribution of displacements. In the presence of strong magnetic field gradients, the diffusion of the water molecules in the tissue causes a signal phase dispersion and subsequent signal attenuation (36) in the direction of the diffusion gradients that is proportional to the distribution of water molecules. From diffusion coefficients D and D_{ref}, acquired at two different temperatures T and T_{ref}, respectively, the temperature change ΔT can be obtained:

$$\Delta T = T - T_{ref} = \frac{kT_{ref}^2}{E_a(D)} \left(\frac{D - D_{ref}}{D_{ref}} \right). \tag{12}$$

It is assumed that the temperature change is small ($\Delta T \ll T_{ref}$) and that E_a is independent of temperature.

The diffusion method has been used to non-invasively measure temperature in vivo (37). Its temperature sensitivity is high, but acquisition times are relatively long and in vivo implementations suffer from an extremely high sensitivity to motion. Single-shot echo planar imaging (37) and line-scanning techniques (38) have been used to reduce the acquisition time and motion sensitivity of this method. An additional complication in vivo is that the temperature dependence of diffusion becomes nonlinear when tissue conditions change. The motility of water in tissue depends on barriers such as cellular structures, proteins, and membranes. Heat induced changes like protein coagulation can, therefore, lead to large changes in the diffusion coefficient. In addition, nonlethal physiological effects such as ischemia in the brain (39) can also lead to large changes in diffusion coefficient. An example of two competing effects, an increase in diffusion due to increasing temperature during thermal ablation and a decrease in diffusion due to tissue coagulation can be appreciated in Fig. 4. The images are acquired during canine prostate ablation with line scan diffusion imaging at 0.5 T.

In tissues with anisotropic diffusion, e.g. muscle fibers, the mobility of water protons is dependent on direction. For accurate temperature measurements, calculations of the full diffusion tensor, which describes the anisotrophy, or the trace, which is rotationally invariant, might be necessary, but these methods require more acquisition time than a diffusion measurement in a single direction. Lipid suppression is necessary in tissues containing fat, because fat has a different change in diffusion coefficient with temperature. Temperature measurements in fat are difficult due to the low diffusion coefficient in fat. A temperature gradient within a single voxel can cause phase dispersion due to PRF changes that may decrease

the signal independent from D. This is a larger problem with diffusion that T_1-mapping since the diffusion images are acquired at considerably longer echo times. Using spin-echo methods is, therefore, recommended to measure the diffusion coefficient. Apart from SNR advantages at high field and changes in relaxation times, temperature imaging based on the diffusion coefficient is independent of field strength.

Magnetization Transfer

Magnetization transfer (MT) techniques use a spectrally selective RF pulse to saturate protons in macromolecules and water molecules that are bound to macromolecules. These protons are normally not visible due to their very short T_2* relaxation times. During the pulse sequence, the saturated protons may enter the free pool of protons, primarily water, or may transfer their magnetization to free water protons. This results in a decrease in the MR visible signal in areas of macromolecules affected by magnetization transfer. Because these MT exchange processes are temperature dependent, they can potentially be used for temperature measurements (30, 40). However, the sensitivity of this method is limited and strongly tissue dependent.

PRF Shift of Water Protons

The temperature sensitivity of the proton resonance frequency (PRF) was first observed by Hindman in 1966 (41) while studying the intermolecular forces and hydrogen bond formation between water molecules. It was first implemented for spectroscopy and later adapted for MR-temperature monitoring by Ishihara *et al*. (42) and De Porter *et al*. (43,44).

The resonance frequency of a nucleus in a molecule is determined by the local magnetic field it experiences. The field at the nucleus can be written as

$$B_{loc}=B_0 - B_{0s}=(1 - s)B_0, \tag{13}$$

where s is called the *shielding constant* or *screening constant* and is dependent on the chemical environment. (Note that the shielding constant is often denoted σ in the literature. In this paper it is denoted s and the symbol σ is used for the standard deviation.) As a result of the nuclear shielding, the resonance frequency becomes

$$\omega=\gamma B_0(1 - s). \tag{14}$$

More details on chemical shift and nuclear shielding can be found in (42).

In water molecules the hydrogen nuclei ^{1}H are screened from the macroscopic field by the electrons of the molecule. An ^{1}H nucleus in a free H_2O molecule is screened more efficiently by the electron cloud than a nucleus in a H_2O molecule which is hydrogen bonded to another molecule. Hydrogen bonds between neighboring molecules distort the electronic configuration of the molecules, which reduces the electronic screening. The fraction and the nature of the hydrogen bonds in water vary with temperature (46). As the temperature increases, the hydrogen bonds stretch, bend (41), and break (47), i.e. on average the H_2O molecules spend less time in a hydrogen-bonded state. Consequently, there is more electron screening of the ^{1}H nucleus, and thus a lower local magnetic field B_{loc} and a lower proton resonance frequency. Because of its physical origins on hydrogen bonding among water molecules, electron screening is considered to be a microscopic effect. A detailed description of these processes is given in Refs. (41) and (47).

The temperature dependent component varies linearly with temperature in the temperature range of interest for thermal ablation and can be described as:

$$s_T(T)=\alpha T. \tag{15}$$

The average electron-screening constant of pure H_2O varies approximately linearly with temperature by about $-1.03 \pm 0.02 * 10^{-8}$/°C over a wide range in temperatures from −15°C to 100°C (41), including the temperature range of interest for interventional procedures.

Temperature imaging based on the PRF shift has evolved into two techniques, spectroscopic imaging and phase mapping methods, that will be separately discussed in the following sections.

Spectroscopic Imaging using the PRF Shift

Proton spectroscopic imaging, like PRF shift thermometry using phase mapping, utilizes the temperature induced water proton chemical shift. Here, the frequency shift is calculated from the MR spectra. The shift is measured between the water peak and a reference peak that remains constant with temperature, such as lipids (48) or N-acetyl-aspartate in the brain (49). This internal reference makes spectroscopic methods relatively immune to field drifts and inter-scan motion, and allows for absolute temperature measurements (49), which have been demonstrated in the human brain (50).

Proton chemical shift imaging (CSI) sequences have been shown to measure absolute temperature distributions within one minute or less and a spatial resolution of 3–4 mm (51). Different acquisition methods have been proposed for spectroscopic temperature measurements, such as single voxel spectroscopy, magnetic resonance spectroscopic imaging (MRSI), echo planar spectroscopic imaging (EPSI), and line scan echo planar spectroscopic imaging (LSPESI) (52).

The ability of spectroscopic imaging to determine absolute temperatures makes it a unique tool for noninvasive temperatures measurements, but has currently limited applicability for realtime temperature monitoring, due to its low temporal and spatial resolution. For more details on the different spectroscopic PRF shift thermometry methods, an excellent review has recently been given by Kuroda (52).

Phase Mapping using the PRF Shift

MRI-derived temperature maps can be constructed using a gradient-recalled echo (GRE) imaging sequence (42) by measuring the phase change resulting from the temperature-dependent change in resonance frequency. Figure 5 shows the use of this method for temperature monitoring during FUS ablation of a uterine fibroid.

In order to eliminate temperature-independent contributions, e.g. due to B_0 field inhomogeneities, one or more images are usually acquired before heating and subtracted from images during heating. The phase difference images are proportional to the temperature-dependent PRF change and the echo time TE and can be converted to a temperature change by

$$\Delta T=\frac{\varphi(T)-\varphi(T_0)}{\gamma\alpha B_0 TE}, \tag{16}$$

where $\varphi(T)$ is the phase in the current image, $\varphi(T_0)$ is the phase of a reference (baseline) image at a known temperature, γ is the gyromagnetic ratio, α is the PRF change coefficient, B_0 is the magnetic field strength, and TE is the echo time.

The echo time TE can be optimized to increase the phase contrast-to-noise ratio and thereby the temperature accuracy, which is identical to the standard deviation in the temperature image σ_T. In a GRE sequence, the temperature-dependent phase difference signal-to-noise ratio, $SNR_{\Delta\varphi}$, is estimated as follows:

$$SNR_{\Delta\varphi}=\frac{|\Delta\varphi(\Delta T)|}{\sigma_{\Delta\varphi}} \tag{17}$$

where $\Delta\varphi/(\Delta T)$ is the phase difference and $\sigma_{\Delta\varphi}$ is the standard deviation of the phase difference image. With $\sigma_{\Delta\varphi} = \sigma/A$, where A is the signal amplitude, the phase difference SNR is directly proportional to the signal intensity:

$$SNR_{\Delta\varphi} \propto |\Delta\varphi(\Delta T)| \cdot A \tag{18}$$

The GRE signal intensity, A, is dependent on tissue parameters, ρ, T_1 and T_2*, as well as the imaging parameters of the GRE sequence, TE, TR, and flip angle. Assuming the tissue parameters are relatively constant, the signal intensity only depends on the imaging parameters. The GRE signal decreases exponentially with increasing TE with time constant T_2*, which accounts for the transverse relaxation and dephasing of the magnetization vector. The phase shift, on the other hand, increases linearly with TE. The $SNR_{\Delta\varphi}$ dependence on the echo time can then be written as:

$$SNR_{\Delta\varphi} \propto TE\, e^{-\frac{TE}{T_2^*}} \tag{19}$$

Differentiating Eq. 19 with respect to TE yields the optimal TE in the temperature dependent phase imaging at TE = T_2* (27,51).

There are a number of other effects that can influence temperature measurements with the proton resonance frequency, such as the composition of the tissue, the susceptibility, the electrical conductivity, and external field drift, which will be briefly summarized here.

Different Tissue Types—It has been shown, that except for adipose tissue, the PRF thermal coefficient is tissue type independent and exhibits only a small dependence on thermal history even when tissue has been coagulated (53,54). Many authors have performed calibration experiments of the temperature dependence of the water PRF shift and most found values between −0.009 and −0.01 ppm/°C (55), in agreement with the pure water value of −0.01 ppm/°C (41). A few studies have found substantially different values, which could be associated with changes in susceptibility or electrical conductivity (discussed later). A recent review of ex vivo and in vivo validation studies for temperature imaging with water PRF shift that discusses the different results has been given by McDannold (55).

The tissue type independence of the PRF shift is only true for aqueous tissues. In water, the dependence of the PRF on temperature is attributed to changes in the hydrogen bonds, which are absent in fat (41). Therefore, the temperature dependence in adipose tissue is almost completely determined by susceptibility effects (details below). The resulting temperature

sensitivity of fat is some orders of magnitude smaller (54), indicating that thermometry inside fatty tissue is difficult.

The fact that the lipid resonance frequency is almost temperature independent poses an important problem for temperature measurements using PRF. Many biological tissues are composed of both water and fat (43). The presence of lipids modifies the phase difference obtained in the thermometry experiment and thus leads to temperature errors. To overcome this problem, lipid suppression (56,57) or selective excitation are commonly used on high field scanners. However, at field strength of 0.5 T and below, chemically selective excitation or suppression is difficult due to the small spectral shift between water and fat.

Temperature Dependence of the Susceptibility—An important complication is the fact that the local magnetic flux density will also change with temperature (58) as a result of the temperature dependence of the susceptibility constant χ_0, as seen in Eqs. 1 and 2. If this temperature dependence of χ_0 is taken into account, Eq. 13 has to be rewritten as (59):

$$B_{loc} \cong \left(1 - \frac{2\chi(T)}{3} - s(T)\right) B_{mac} \tag{20}$$

where higher-order terms in χ and s have been neglected. T is the temperature inside the object. The term B_{mac} describes the macroscopic magnetic flux density, which appears when an object with a volume susceptibility χ is placed in a uniform magnetic flux density B_0. B_{mac} is a function of the external field B_0, the geometry of the object, the susceptibility distribution within and outside the object and can be determined from Maxwell's equations.

If B_{loc} from Eq. 20 is used to calculate the temperature change, the local phase is not only dependent on the temperature dependent chemical shift, but also becomes a function of the temperature dependent susceptibility. For the temperature range of interest, the temperature dependence of both s and χ can be approximated as linear. The susceptibility change with temperature is 0.0026 ppm/°C in pure water and 0.0016 ppm/°C for muscle tissue in the temperature range of 30°C to 45°C (44). But whereas the temperature dependence of the chemical shift is nearly constant for all tissue types (with the exception of adipose tissue), the temperature dependence of the susceptibility is tissue-type dependent (60).

For pure water and tissues with high water content such as muscle tissue, the temperature dependence of the screening constant is much larger than that of the susceptibility. Because of this, the temperature dependence of the susceptibility constant has only a small effect on thermometry applications in these tissues and errors remain within 10% of the temperature variation (44). Therefore, most implementations of PRF thermometry in aqueous tissue assume only temperature effects of the screening constant. More details about the effect of temperature dependent susceptibility in the PRF method can be found in De Poorter *et al*. (44). Peters *et al*. (61) have also investigated the temperature induced changes in the volume magnetic susceptibility and found a dependence on the orientation and geometry of the heat-delivery device and its associated heat pattern.

Electrical Conductivity—A study by Peters and Henkelman (62) has shown that under certain experimental conditions, the temperature-induced phase shift may not scale with the TE setting, as suggested by Eq. 16. This phase shift offset originates from temperature-induced changes in the electrical conductivity of tissue. The amplitude attenuation and phase retardation that a time-varying inductive field $B_1(t)$, such as the RF pulse, experiences in an electrically conductive material determines the distribution of tip angles of the spins in the object and the variation of the transverse magnetization phase with depth (63). Changes in electrical

conductivity of tissue with temperature thus change the phase retardation. Because the phase retardation is a function of depth, the effect primarily occurs when relatively large volumes are uniformly heated. Since thermal ablation therapies generally use small heating sources and a relatively long TE, this phenomenon is mostly insignificant when treatment is monitored in practice. However, in hyperthermia the phase retardation effect should be more of a concern. In addition, uniform heating of large volumes is often used for measurement of the PRF coefficient, which might explain discrepancies in the PRF-thermal coefficient of water reported in the literature, e.g. (53,55,64).

Phase Drift—The PRF method needs temporal stability of the external magnetic flux. A drift of the external magnetic field, which can be caused for example by intense gradient utilization (65), results in an extra phase shift commonly referred to as phase drift. This phase drift causes incorrect temperature readings during a thermal procedure. However, the phase drift can be measured with a reference phantom that remains at a fixed temperature if the external field drift is uniform over the image (66). If necessary, a correction for linear phase drift can be applied, by fitting a linear plane to at least three reference phantoms (43). Recently, a method has been suggested that uses the apparent diffusion coefficient in combination with the PRF to yield drift corrected temperature maps (67). A number of reconstruction methods, primarily developed for motion insensitivity and discussed later in this paper, automatically correct for external field drift.

Temperature-Sensitive Contrast Agents

In recent years, temperature-sensitive contrast agents have gained interest for guiding thermal therapies, including paramagnetic thermosensitive liposomes, paramagnetic lanthanide complexes, and spin transition molecular materials.

Paramagnetic thermosensitive liposomes are composed of a gadolinium or manganese-based compound enclosed by a phospholipid membrane (68). Below a distinct gel-to-liquid crystalline phase transition temperature (T_m), the liposomes do not allow water exchange through the membrane. Above T_m the membrane becomes water permeable, yielding fast exchange conditions and therefore relaxation enhancement. T_m of the phospholipid can be adjusted by changing the length and saturation of the hydrocarbon chain. The strong non-linear relationship between measured effect and temperature does not allow continuous temperature measurement, but absolute temperature can be measured at T_m. A recent review on paramagnetic thermosensitive liposomes is given by Lindner *et al*. (69). In vivo application has been demonstrated in animals (70,71). In addition to their use as contrast agents, paramagnetic thermosensitive contrast agents play an important role in local drug delivery research.

Different paramagnetic lanthenide complexes have been proposed for temperature imaging, such as $DOTMA^-$, $TmDOTMA^-$, and others. These complexes have chemical shifts many times more sensitive than the water ^1H shift, e.g. $TmDOTMA^-$ has a temperature coefficient of 0.57 ppm/°C, which is nearly 60 times that of water. In order to image the methyl ^1H signal from $TmDOTMA^-$, excellent water suppression is necessary, resulting in imaging times of several minutes (72,73). Limitations for in vivo applications are the required concentration of the agent and low SNR.

Another kind of paramagnetic lanthanide complex has been investigated for temperature imaging. Here the agent itself is not measured, but the change of the bulk water signal intensity as a results of chemical exchange saturation transfer (CEST). The paramagnetic agents are, therefore, referred to as PARACEST agents (74). A large chemical shift between water and agents allows to easily saturate the PARACEST spins leading to little off-resonance saturation of the bulk water signal. Because the exchange rate is directly related to temperature via the

Arrhenius equation, the temperature can be measured if the agent concentration is known. However, this is difficult for in vivo applications where the agent concentration is usually unknown. Since the chemical shift of the paramagnetic lanthenide complexes itself is temperature sensitive (as described in the previous paragraph), images can be acquired with a series of selective saturation pulses that are varied over a range of frequencies that cover the resonance frequency of the agent. The frequency offset that causes the lowest signal is determined on a pixel-by-pixel basis and determines the temperature change. Although the agent concentration does not have to be known for this method, the imaging time is long (in the order of several minutes), especially if the temperature range to be measured is large (75).

Spin transition molecular materials are bistable molecular complexes that switch from a spin S=0 diamagnetic state to a S=2 paramagnetic state at a temperature given by its chemical composition (76). Others have investigated contrast mechanisms based on the Curie Temperature (T_C), at which a ferromagnetic substance loses its ability to possess a net magnetization in the absence of an external magnetic field and becomes paramagnetic (77). These contrast mechanisms have been demonstrated in vitro. For in vivo use, nontoxic compounds need to be developed and their transition temperature has to be adjustable.

Temperature-sensitive contrast agents have gained interest in recent years and have been demonstrated in various animal experiments. However, MR-thermometry based on temperature-sensitive contrast agents is dependent on a homogeneous accumulation and retention in the target tissue, which is often difficult to achieve, for example in necrotic tumors. Therefore, temperature measurements might not be representative for the temperature distribution of the tumor. Also, non-toxicity of the agents has to be ensured for in vivo applications.

Combined Methods

In order to increase temperature accuracy, the combination of different methods into a single acquisition has been investigated, e.g. T_1 and M_0 (78–80) or T_1 and PRF (27). However, due to the tissue-type dependence of the T_1 method, the combination of T_1 and PRF can also become tissue-type dependent. If two echoes are acquired in a single acquisition, the short TE echo can be used for qualitative T_1 based temperature mapping and the long TE for PRF-based temperature mapping. This is a reasonable approach in breast tissue, a heterogeneous mixture of fatty and glandular tissue, because temperature measurements in fat are not possible with the PRF method. However, in this case, care has to be taken when evaluating quantitative temperature measurements with the PRF method, because pixels with a partial volume of fat will give a temperature overestimation or underestimation, depending on the echo time TE (81).

Advanced temperature imaging with PRF phase mapping

From the methods presented here, PRF-based temperature mapping has found by far the greatest acceptance for many applications at mid-field (0.5 – 1.5 T), as a large number of papers published in the past years has shown. This part of the paper will discuss advances in PRF-based phase mapping: rapid imaging techniques, motion artifacts and motion reduction techniques, reconstruction algorithms, and real-time feedback.

Pulse Sequences

Ideally, MR thermometry provides high temporal and spatial resolution to precisely monitor the temperature distribution within the targeted tissue and predicts the outcome of the thermal treatment. For thermal therapies, real-time can be defined as an update time that is small compared to a significant change in temperature during treatment. Depending on the

application the update time can vary considerably: in hyperthermia an adequate update time can be in the order of a minute or more (52), whereas in thermal ablation an update time of one second or less can be necessary. For slow update rates, imaging times are not an issue, but for long exposure times (82), effects such as tissue motion can become a problem, which will be discussed in the next section. In this section, imaging sequences for rapid temperature monitoring will be introduced. As acceleration in many cases comes at the cost of SNR reduction and increased temperature uncertainty, acquisition parameters for a given fast imaging sequence should be chosen carefully to achieve the optimal compromise for a specific situation.

Fast temperature mapping can be achieved with gradient-echo echoplanar imaging (EPI) or segmented-EPI acquisitions (56,83). Parallel imaging using sensitivity encoding (SENSE) can be added to increase temporal resolution and reduce artifacts due to organ displacement, as demonstrated in animals and human liver (84). The use of generalized autocalibrated partially parallel acquisition (GRAPPA) and k-space inherited parallel acquisition (KIPA) for temperature measurement has also been shown in phantoms (85). Although parallel imaging techniques perturb image phase, relative phase changes, such as those induced by temperature changes, can be reliably measured using reconstruction filters that remain constant across the time series (86).

Because PRF-based temperature imaging is based on gradient echoes with long TE (ideally equal to T_2* of the tissue), conventional gradient echo sequences result in a relatively long TR. If the resulting temporal resolution is inadequate to monitor the thermal treatment, echo shifting can be applied, which leads to a TR < TE in fast gradient echo sequences (57). Echo-shifting can be combined with multi-shot echoplanar imaging, which is then called principles of echo shifting with a train of observations (PRESTO) (87).

The use of spiral or interleaved spiral acquisitions also allows for long echo times without sacrificing temporal resolution (88). It has been noted that spiral acquisitions resulted in sightly higher temperature responses than comparable 2D gradient echo sequences. This could be explained by the difference between the nominal TE at the beginning of the readout (for outward spirals) and the effective TE when high frequencies are sampled, which is longer than in 2D sequences. An additional feature of spiral acquisitions is that the center of k-space is sampled in every acquisition, which can be used as navigators for motion detection (see next section).

Methods using balanced steady-state free-precession (SSFP) for PRF temperature imaging have also been investigated. Because the phase behavior with respect to frequency is highly nonlinear in balanced SSFP, a simple phase to frequency mapping as used in gradient echo imaging is not possible. Determining the frequency as the slope of a linear fit of phases measured at different TEs along an echo train (89), sampling the balanced-SSFP frequency offset curve by excitation with various RF phase angles (90), and linearization of the phase frequency relation by averaging multiple phase-cycled balanced SSFP images (91) are attempts to overcome this problem and have been demonstrated in phantoms. The value of these methods for in vivo applications remains to be determined.

PRF Thermometry and Motion

Motion is the most prevalent problem for temperature monitoring with PRF phase mapping and the main reason that has impeded its acceptance for clinical application in areas that are subject to motion. For temperature monitoring during thermal treatment, motion artifacts can be divided into two categories, intra-scan motion and inter-scan motion, based on the time scale of the motion with respect to the image acquisition time.

Intra-scan motion is caused by movement of an object during MR image acquisition, resulting in a poor quality image with typical blurring and ghosting artifacts. These motion artifacts are not specific to PRF temperature imaging and can be reduced by accelerating the image acquisition, e.g. by methods discussed in the previous section. Trade-offs between acquisition time and SNR and temperature uncertainty have to be considered.

Inter-scan motion occurs due to motion or displacement of an object between the acquisition of consecutive images. As discussed earlier, temperature images obtained using the PRF method are usually reconstructed by calculating the phase difference between a baseline image acquired prior to heating and the current heating image. If motion is present between the acquisition of the images, the images are not registered to the baseline and artifacts in the temperature maps occur. New baseline images cannot be acquired once the thermal procedure has started until the heated region has returned to baseline temperature. Unfortunately, many of the target areas for thermotherapy are in the abdomen, where motion is ubiquitous.

A major source of motion, especially in the upper abdominal organs, is respiration. Respiration not only displaces the organs but also changes the susceptibility field. A calculation method for the magnetic field distribution due to an arbitrary distribution of bulk susceptibility has been given by Salomir *et al*. (92). Even without tissue motion in the imaged region, lung filling can change the background phase enough to render temperature measurements based on subtraction useless. Because treatment durations in thermal therapy are in the order of several minutes, the treatments cannot be performed in a single breathhold. Using multiple breathholds is difficult, because reproducible breathholding is hard to achieve.

But even without respiratory motion, displacement between images can occur. Thermal coagulation leads to structural changes and deformation of the treated tissue, which can be observed ex vivo without any other source of motion present. This heating-induced tissue motion is often not a simple global displacement (82). The tissue swells in three dimensions, causing a local warping of the field distribution at the position of the swelling. In vivo, swelling during the treatment and changes in muscle tension, or peristalsis can also cause tissue displacement. An example of the resulting type of error is demonstrated in Fig. 6, which shows the temperature distribution during canine prostate ablation overlaid onto the corresponding magnitude image. The image was acquired after the thermal ablation ended and the temperature in the prostate had returned to body temperature, such that all areas in the temperature map that appear hot are artifacts caused by tissue displacement.

Different strategies to overcome the problem with motion have been proposed. Some methods are specifically designed for repetitive motion due to respiration and others use a more general approach to deal with non-repetitive motion as well.

In case of respiration, the motion can be monitored with external methods and synchronized with MR imaging such that image acquisition occurs during a stable period of the breathing cycle. Conventional respiratory gating in animals under general anesthesia and mechanical respiration (93) has been successfully used. Respiratory gating during free breathing has also been used (94), but gating can fail when the respiratory cycle is irregular, leading to motion artifacts and errors in the temperature maps (84). Others have described motion detection and movement registration with navigator echoes for displacements of ex vivo tissue (87). However, the use of navigator echoes is restricted to rigid body motion and may not be optimal for complex organ displacements or deformations. A triggered, navigated, multi-baseline method was demonstrated in the liver in vivo with variable respiratory motion (95). This technique uses respiratory triggering, diaphragm position determination with a navigator echo, and the collection of multiple baseline images to generate the temperature maps. For a comparison of some of these methods, Fig. 7 shows temperature maps during laser heating in

the liver of a pig during variable respiratory motion. Recently, methods have been proposed, where the heating images are matched to a set of baseline images based on their non-similarity coefficients (96) or intercorrelation coefficients (97).

A method becomes insensitive both to repetitive and non-repetitive inter-scan motion, if the need of baseline image subtraction is eliminated. One approach, called *referenceless thermometry* or *self-referenced thermometry* tries to estimate the heating from every individual image itself, without a preheating reference scan. The background phase inside the heating region is estimated by fitting a polynomial function to the unwrapped background phase (98) or a complex valued polynomial (99) to the complex image outside the heating region using a weighted least-squares fit. The extrapolation of the polynomial to the heated region serves as the background phase estimate, which is then subtracted from the actual phase. These methods require a heating area that is at least partially surrounded by a non-heated region with sufficient SNR. This is often the case for thermal ablation procedures but not in hyperthermia. Because of echo time dependent phase discontinuities between water and fat regions, which would inhibit polynomial fitting, fat needs to be suppressed or the reconstruction algorithm should be modified to be able to handle both tissue types (100). Figure 8 shows temperature maps in a canine prostate without heating, while light pressure was applied to the animal's abdomen, demonstrating the ability of referenceless thermometry to measure temperature in the presence of tissue motion.

Recently, a method to correct magnetic field disturbances using the signal from fat has been proposed (101). The method uses a similar idea as Ref. (48) but is more robust to suboptimal fat-water separation.

Real-time feedback

Once accurate temperature measurements are achieved during real-time, they can be used as a feedback to adjust the thermal treatment if necessary. Especially when moving organs are treated (e.g. with FUS), real-time feedback is useful to ensure that the correct tissue region is treated.

De Senneville *et al.* (97) have demonstrated an adaptive method with real-time tracking of the target, online motion correction of the temperature maps, and regional temperature control based on PID (proportional, integral, and derivative) control of power and focal spot of the FUS transducer.

Although most temperature monitoring has been done in single or multiple slice acquisition, there are situations when covering a 3D volume is desirable, if the location of the heated region changes due to respiratory motion. However, in many cases isotropic 3D temperature mapping is hardly feasible in real-time. Alternatively, the heating spot can be tracked if the device has active tracking coils or other techniques from catheter tracking might be used (102).

Discussion

In the previous sections MR temperature measurements based on proton density, T_1 and T_2 relaxations times, magnetization transfer, diffusion, proton resonance frequency, and thermosensitive contrast agents have been introduced. With these different temperature-sensitive parameters, MRI has been shown to be an excellent modality to noninvasively monitor thermal therapy to ensure efficacy and safety of the treatment. Temperature monitoring has been successfully demonstrated in vivo and is regularly used in a number of clinical applications mainly in combination with FUS heating. However, a number of challenges remain for MR thermometry to be widely accepted for monitoring thermal procedures. Because the target of many ablation procedures lies in the abdomen, reliable and robust motion-

insensitive acquisition techniques and reconstruction algorithms are indispensable. To date, only T_1, diffusion and PRF have been used for in vivo temperature monitoring during thermal therapy.

Numerous studies have attempted to compare different methods (35,59,66), but because the usefulness of any method depends strongly on the application, the imaged body part, field strength, and other parameters, it is difficult to draw general conclusions. And although the proportionality constant of PRF with temperature appears low compared to T_1 and D, PRF-based methods have resulted in higher precision (103), suggesting that temperature monitoring with the PRF is the most sensitive among endogenous MRI parameters in detecting small temperature changes (104). When field inhomogeneity is poor, e.g. due to an inserted needle or applicator, the PRF method may not be as accurate as diffusion or T_1 relaxation which can be acquired with spin echo methods. In addition, at very low field strength the PRF method may be less sensitive than diffusion or T_1 relaxation because of its linear dependence on field strength.

Generally, to avoid errors from fat, lipid suppression is necessary when T_1, D, or PRF methods are employed in tissues that contain fat. All three methods require very good registration to correct for displacements between scans. In addition, the diffusion method is particularly sensitive to motion artifacts during the scan.

A major need is a reliable method to measure absolute temperature with good spatial and temporal resolution. Even if the temporal resolution is still too low for real-time monitoring, a fast PRF phase mapping sequence could be interspersed with absolute temperature measurements. This would allow taking new baseline images at any time during the procedure when the absolute temperature is measured. This would greatly alleviate the requirement for motion insensitivity and could avoid having to terminate the procedure in case of tissue motion. In cases where cooling is applied to protect sensitive structures near the heated area, absolute temperature measurement would be helpful to prevent measurement errors resulting from baseline images not taken at body temperature.

The fact that PRF phase mapping cannot be used to measure temperature in lipids poses significant problems for treatment of organs that contain large amounts of fat, (e.g. breast and skin). Skin burns can be a problem in FUS procedures, because the skin interface lies in the near field of the ultrasound beam. Without the ability to monitor temperature in the fatty skin layer, skin burns can occur.

Because PRF phase mapping gives a linear relationship to temperature and is not influenced by tissue changes, this methods provides accurate temperature measurements in the temperature range of interest for thermal ablation. This linearity is usually considered an advantage when different MR temperature methods are compared. However, to be able to control the treatment outcome, it is not only necessary to accurately measure the temperature during treatment, but also to be able to relate treatment temperature to actual thermal tissue damage. The nonlinearity of measurements with T_1, T_2, diffusion, and MT might provide a more direct measure of tissue changes as a response to the thermal treatment. MR elastography has also been used to detect changes in tissue stiffness caused by ablation (105). Because tissue microstructure undergoes major changes during thermal coagulation, it is hypothesized that these MR parameters provide a more direct estimate of cell death. A quantitative interpretation of the changes of these MR parameters is complicated because the term thermal coagulation encompasses multiple different responses of tissue to heating at different temperatures. These effects include enzyme deactivation and reversible cell injury, cell shrinkage and hyperchromasia, cell death and denaturation of proteins (2), but it is likely that MR parameters are only sensitive to a subset of these tissue changes (33).

Conclusion

The background and recent progress in the field of MR thermometry for monitoring thermal therapy were reviewed. A number of temperature-sensitive MR parameters make MRI a unique tool to noninvasively measure temperature in vivo. Furthermore, MRI can also provide information about the response of the tissue to the thermal treatment, although this is beyond the scope of this paper. Reliable temperature measurement in fat and in the presence of motion as well as absolute temperature quantification remain greatly anticipated technologies.

Acknowledgments

We would like to thank Thomas J. Vogl and Nathan McDannold for providing images of their work for this review.

Grant Sponsor: NIH (R01 CA077677, RO1 CA111981, RO1 CA121163)

References

1. Kim JH, Hahn EW. Clinical and biological studies of localized hyperthermia. Cancer Res 1979;39:2258–2261. [PubMed: 445426]
2. Thomsen S. Pathologic analysis of photothermal and photomechanical effects of laser-tissue interactions. Photochem Photobiol 1991;53:825–835. [PubMed: 1886941]
3. Sapareto SA, Dewey WC. Thermal dose determination in cancer therapy. Int J Radiat Oncol Biol Phys 1984;10:787–800. [PubMed: 6547421]
4. Dewhirst MW, Viglianti BL, Lora-Michiels M, Hanson M, Hoopes PJ. Basic principles of thermal dosimetry and thermal thresholds for tissue damage from hyperthermia. Int J Hyperthermia 2003;19:267–294. [PubMed: 12745972]
5. Mack MG, Straub R, Eichler K, Engelmann K, Zangos S, Roggan A, Woitaschek D, Bottger M, Vogl TJ. Percutaneous MR imaging-guided laser-induced thermotherapy of hepatic metastases. Abdom Imaging 2001;26:369–374. [PubMed: 11441548]
6. Hokland SL, Pedersen M, Salomir R, Quesson B, Stodkilde-Jorgensen H, Moonen CTW. MRI-guided focused ultrasound: methodology and applications. IEEE Trans Med Imaging 2006;25:723–731. [PubMed: 16768237]
7. Diederich CJ, Nau WH, Ross AB, Tyreus PD, Butts K, Rieke V, Sommer G. Catheter-based ultrasound applicators for selective thermal ablation: progress towards MRI-guided applications in prostate. Int J Hyperthermia 2004;20:739–756. [PubMed: 15675669]
8. Vigen KK, Jarrard J, Rieke V, Frisoli J, Daniel BL, Butts Pauly K. In vivo porcine liver radiofrequency ablation with simultaneous mr temperature imaging. J Magn Reson Imaging 2006;23:578–584. [PubMed: 16508928]
9. Zhang Q, Chung YC, Lewin JS, Duerk JL. A method for simultaneous RF ablation and MRI. J Magn Reson Imaging 1998;8:110–114. [PubMed: 9500269]
10. Botnar RM, Steiner P, Dubno B, Erhart P, von Schulthess GK, Debatin JF. Temperature quantification using the proton frequency shift technique: In vitro and in vivo validation in an open 0.5 tesla interventional MR scanner during RF ablation. J Magn Reson Imaging 2001;13:437–444. [PubMed: 11241819]
11. Moriarty JA, Chen JC, Purcell CM, Ang LC, Hinks RS, Peters RD, Henkelman RM, Plewes DB, Bronskill MJ, Kucharczyk W. MRI monitoring of interstitial microwave-induced heating and thermal lesions in rabbit brain in vivo. J Magn Reson Imaging 1998;8:128–135. [PubMed: 9500272]
12. Quesson B, de Zwart JA, Moonen CT. Magnetic resonance temperature imaging for guidance of thermotherapy. J Magn Reson Imaging 2000;12:525–533. [PubMed: 11042633]
13. Abragam, A. The principles of nuclear magnetism. Vol. Chapter I. Oxford: The Claredon Press; 1983.
14. Johnson, F.; Eyring, H.; Stover, B. Theory of rate processes in biology and medicine. New York: John Wiley & Sons; 1974.
15. Chen J, Daniel BL, Pauly KB. Investigation of proton density for measuring tissue temperature. J Magn Reson Imaging 2006;23:430–434. [PubMed: 16463298]

16. Gultekin DH, Gore JC. Temperature dependence of nuclear magnetization and relaxation. J Magn Reson 2005;172:133–141. [PubMed: 15589416]
17. Bloembergen N, Purcell EM, Pound RV. Relaxation effects in nuclear magnetic resonance absorption. Physical Review 1948;73:679–712.
18. Parker DL. Applications of NMR imaging in hyperthermia: an evaluation of the potential for localized tissue heating and noninvasive temperature monitoring. IEEE Trans Biomed Eng 1984;31:161–167. [PubMed: 6724602]
19. Parker DL, Smith V, Sheldon P, Crooks LE, Fussell L. Temperature distribution measurements in two-dimensional NMR imaging. Med Phys 1983;10:321–325. [PubMed: 6877179]
20. Bottomley PA, Foster TH, Argersinger RE, Pfeifer LM. A review of normal tissue hydrogen NMR relaxation times and relaxation mechanisms from 1–100 MHz: dependence on tissue type, NMR frequency, temperature, species, excision, and age. Med Phys 1984;11:425–448. [PubMed: 6482839]
21. Cline HE, Schenck JF, Watkins RD, Hynynen K, Jolesz FA. Magnetic resonance-guided thermal surgery. Magn Reson Med 1993;30:98–106. [PubMed: 8371680]
22. Lewa CJ, Ma jewska Z. Temperature relationships of proton spin-lattice relaxation time T1 in biological tissues. Bull Cancer 1980;67:525–530. [PubMed: 6260272]
23. Cline HE, Hynynen K, Hardy CJ, Watkins RD, Schenck JF, Jolesz FA. MR temperature mapping of focused ultrasound surgery. Magn Reson Med 1994;31:628–636. [PubMed: 8057815]
24. Matsumoto R, Oshio K, Jolesz FA. Monitoring of laser and freezing-induced ablation in the liver with T1-weighted MR imaging. J Magn Reson Imaging 1992;2:555–562. [PubMed: 1392248]
25. Hynynen K, McDannold N, Mulkern RV, Jolesz FA. Temperature monitoring in fat with MRI. Magn Reson Med 2000;43:901–904. [PubMed: 10861887]
26. Matsumoto R, Mulkern RV, Hushek SG, Jolesz FA. Tissue temperature monitoring for thermal interventional therapy: comparison of T1-weighted MR sequences. J Magn Reson Imaging 1994;4:65–70. [PubMed: 8148558]
27. Cline HE, Hynynen K, Schneider E, Hardy CJ, Maier SE, Watkins RD, Jolesz FA. Simultaneous magnetic resonance phase and magnitude temperature maps in muscle. Magn Reson Med 1996;35:309–315. [PubMed: 8699941]
28. Nelson TR, Tung SM. Temperature dependence of proton relaxation times in vitro. Magn Reson Imaging 1987;5:189–199. [PubMed: 3041151]
29. Peller M, Reinl HM, Weigel A, Meininger M, Issels RD, Reiser M. T1 relaxation time at 0.2 Tesla for monitoring regional hyperthermia: feasibility study in muscle and adipose tissue. Magn Reson Med 2002;47:1194–1201. [PubMed: 12111966]
30. Young IR, Hand JW, Oatridge A, Prior MV. Modeling and observation of temperature changes in vivo using MRI. Magn Reson Med 1994;32:358–369. [PubMed: 7984068]
31. Fung BM, Durham DL, Wassil DA. The state of water in biological systems as studied by proton and deuterium relaxation. Biochim Biophys Acta 1975;399:191–202. [PubMed: 1148275]
32. Vogl TJ, Straub R, Zangos S, Mack MG, Eichler K. MR-guided laser-induced thermotherapy (LITT) of liver tumors: experimental and clinical data. Int J Hyperthermia 2004;20:713–724. [PubMed: 15675667]
33. Graham SJ, Bronskill MJ, Henkelman RM. Time and temperature dependence of MR parameters during thermal coagulation of ex vivo rabbit muscle. Magn Reson Med 1998;39:198–203. [PubMed: 9469702]
34. Gandhi, S.; Daniel, BL.; Butts, K. Temperature dependence of relaxation times in bovine adipose tissue. Proceedings 6th ISMRM; Sydney, Australia. 1998. p. 701
35. Le Bihan D, Delannoy J, Levin RL. Temperature mapping with MR imaging of molecular diffusion: application to hyperthermia. Radiology 1989;171:853–857. [PubMed: 2717764]
36. Stejskal EO, Tanner JE. Spin diffusion measurements - spin echoes in presence of a time-dependent field gradient. Journal of Chemical Physics 1965;42:288–292.
37. Bleier AR, Jolesz FA, Cohen MS, Weisskoff RM, Dalcanton JJ, Higuchi N, Feinberg DA, Rosen BR, McKinstry RC, Hushek SG. Real-time magnetic resonance imaging of laser heat deposition in tissue. Magn Reson Med 1991;21:132–137. [PubMed: 1943670]

38. Morvan D, Leroy-Willig A, Malgouyres A, Cuenod CA, Jehenson P, Syrota A. Simultaneous temperature and regional blood volume measurements in human muscle using an MRI fast diffusion technique. Magn Reson Med 1993;29:371–377. [PubMed: 8450745]
39. Moseley ME, Cohen Y, Mintorovitch J, Chileuitt L, Shimizu H, Kucharczyk J, Wendland MF, Weinstein PR. Early detection of regional cerebral ischemia in cats: comparison of diffusion- and T2-weighted MRI and spectroscopy. Magn Reson Med 1990;14:330–346. [PubMed: 2345513]
40. Graham SJ, Stanisz GJ, Keco jevic A, Bronskill MJ, Henkelman RM. Analysis of changes in MR properties of tissues after heat treatment. Magn Reson Med 1999;42:1061–1071. [PubMed: 10571927]
41. Hindman JC. Proton resonance shift of water in gas and liquid states. Journal of Chemical Physics 1966;44:4582–4592.
42. Ishihara Y, Calderon A, Watanabe H, Okamoto K, Suzuki Y, Kuroda K, Suzuki Y. A precise and fast temperature mapping using water proton chemical shift. Magn Reson Med 1995;34:814–823. [PubMed: 8598808]
43. De Poorter J, De Wagter C, De Deene Y, Thomsen C, Stahlberg F, Achten E. Noninvasive MRI thermometry with the proton resonance frequency (PRF) method: in vivo results in human muscle. Magn Reson Med 1995;33:74–81. [PubMed: 7891538]
44. De Poorter J. Noninvasive MRI thermometry with the proton resonance frequency method: study of susceptibility effects. Magn Reson Med 1995;34:359–367. [PubMed: 7500875]
45. Hore, P. Nuclear magnetic resonance. Oxford: Oxford University Press; 1995.
46. Nemethy G, Scheraga Ha. Structure of water and hydrophobic bonding in proteins. 1. a model for thermodynamic properties of liquid water. Journal of Chemical Physics 1962;36:3382–3392.
47. Schneider WG, Bernstein HJ, Pople JA. Proton magnetic resonance chemical shift of free (gaseous) and associated (liquid) hydride molecules. Journal of Chemical Physics 1958;28:601–607.
48. Kuroda K, Oshio K, Chung AH, Hynynen K, Jolesz FA. Temperature mapping using the water proton chemical shift: a chemical shift selective phase mapping method. Magn Reson Med 1997;38:845–851. [PubMed: 9358461]
49. Cady EB, D'Souza PC, Penrice J, Lorek A. The estimation of local brain temperature by in vivo 1H magnetic resonance spectroscopy. Magn Reson Med 1995;33:862–867. [PubMed: 7651127]
50. Marshall I, Karaszewski B, Wardlaw JM, Cvoro V, Wartolowska K, Armitage PA, Carpenter T, Bastin ME, Farrall A, Haga K. Measurement of regional brain temperature using proton spectroscopic imaging: validation and application to acute ischemic stroke. Magn Reson Imaging 2006;24:699–706. [PubMed: 16824964]
51. Kuroda K, Mulkern RV, Oshio K, Panych LP, Nakai T, Moriya T, Okuda S, Hynynen K, Jolesz FA. Temperature mapping using the water proton chemical shift: self-referenced method with echo-planar spectroscopic imaging. Magn Reson Med 2000;43:220–225. [PubMed: 10680685]
52. Kuroda K. Non-invasive MR thermography using the water proton chemical shift. Int J Hyperthermia 2005;21:547–560. [PubMed: 16147439]
53. Peters RD, Hinks RS, Henkelman RM. Ex vivo tissue-type independence in proton-resonance frequency shift MR thermometry. Magn Reson Med 1998;40:454–459. [PubMed: 9727949]
54. Kuroda K, Oshio K, Mulkern RV, Jolesz FA. Optimization of chemical shift selective suppression of fat. Magn Reson Med 1998;40:505–510. [PubMed: 9771566]
55. McDannold N. Quantitative MRI-based temperature mapping based on the proton resonant frequency shift: review of validation studies. Int J Hyperthermia 2005;21:533–546. [PubMed: 16147438]
56. Weidensteiner C, Quesson B, Caire-Gana B, Kerioui N, Rullier A, Trillaud H, Moonen CT. Real-time MR temperature mapping of rabbit liver in vivo during thermal ablation. Magn Reson Med 2003;50:322–330. [PubMed: 12876709]
57. de Zwart JA, Vimeux FC, Delalande C, Canioni P, Moonen CT. Fast lipid-suppressed MR temperature mapping with echo-shifted gradient-echo imaging and spectral-spatial excitation. Magn Reson Med 1999;42:53–59. [PubMed: 10398950]
58. Schenck JF. The role of magnetic susceptibility in magnetic resonance imaging: MRI magnetic compatibility of the first and second kinds. Med Phys 1996;23:815–850. [PubMed: 8798169]

59. Stollberger R, Ascher PW, Huber D, Renhart W, Radner H, Ebner F. Temperature monitoring of interstitial thermal tissue coagulation using MR phase images. J Magn Reson Imaging 1998;8:188–196. [PubMed: 9500279]
60. Young IR, Ha jnal JV, Roberts IG, Ling JX, Hill-Cottingham RJ, Oatridge A, Wilson JA. An evaluation of the effects of susceptibility changes on the water chemical shift method of temperature measurement in human peripheral muscle. Magn Reson Med 1996;36:366–374. [PubMed: 8875406]
61. Peters RD, Hinks RS, Henkelman RM. Heat-source orientation and geometry dependence in proton-resonance frequency shift magnetic resonance thermometry. Magn Reson Med 1999;41:909–918. [PubMed: 10332873]
62. Peters RD, Henkelman RM. Proton-resonance frequency shift MR thermometry is affected by changes in the electrical conductivity of tissue. Magn Reson Med 2000;43:62–71. [PubMed: 10642732]
63. Bottomley PA, Andrew ER. RF magnetic field penetration, phase shift and power dissipation in biological tissue: implications for NMR imaging. Phys Med Biol 1978;23:630–643. [PubMed: 704667]
64. MacFall JR, Prescott DM, Charles HC, Samulski TV. 1H MRI phase thermometry in vivo in canine brain, muscle, and tumor tissue. Med Phys 1996;23:1775–1782. [PubMed: 8946373]
65. El-Sharkawy AM, Schar M, Bottomley PA, Atalar E. Monitoring and correcting spatio-temporal variations of the MR scanner's static magnetic field. MAGMA 2006;19:223–236. [PubMed: 17043837]
66. De Poorter J, De Wagter C, De Deene Y, Thomsen C, Stahlberg F, Achten E. The proton-resonance-frequency-shift method compared with molecular-diffusion for quantitative measurement of 2-dimensional time-dependent temperature distribution in a phantom. Journal of Magnetic Resonance Series B 1994;103:234–241.
67. Das SK, Macfall J, McCauley R, Craciunescu O, Dewhirst MW, Samulski TV. Improved magnetic resonance thermal imaging by combining proton resonance frequency shift (PRFS) and apparent diffusion coefficient (ADC) data. Int J Hyperthermia 2005;21:657–667. [PubMed: 16278169]
68. Fossheim SL, Il'yasov KA, Hennig J, Bjornerud A. Thermosensitive paramagnetic liposomes for temperature control during MR imaging-guided hyperthermia: in vitro feasibility studies. Acad Radiol 2000;7:1107–1115. [PubMed: 11131055]
69. Lindner LH, Reinl HM, Schlemmer M, Stahl R, Peller M. Paramagnetic thermosensitive liposomes for MR-thermometry. Int J Hyperthermia 2005;21:575–588. [PubMed: 16147441]
70. Frich L, Bjornerud A, Fossheim S, Tillung T, Gladhaug I. Experimental application of thermosensitive paramagnetic liposomes for monitoring magnetic resonance imaging guided thermal ablation. Magn Reson Med 2004;52:1302–1309. [PubMed: 15562487]
71. McDannold N, Fossheim SL, Rasmussen H, Martin H, Vykhodtseva N, Hynynen K. Heat-activated liposomal MR contrast agent: initial in vivo results in rabbit liver and kidney. Radiology 2004;230:743–752. [PubMed: 14764890]
72. Pakin SK, Hekmatyar SK, Hopewell P, Babsky A, Bansal N. Non-invasive temperature imaging with thulium 1,4,7,10-tetraazacyclododecane-1,4,7,10-tetramethyl-1,4,7,10-tetraacetic acid (TmDOTMA-). NMR Biomed 2006;19:116–124. [PubMed: 16404728]
73. Hekmatyar SK, Kerkhoff RM, Pakin SK, Hopewell P, Bansal N. Noninvasive thermometry using hyperfine-shifted MR signals from paramagnetic lanthanide complexes. Int J Hyperthermia 2005;21:561–574. [PubMed: 16147440]
74. Woessner DE, Zhang S, Merritt ME, Sherry AD. Numerical solution of the bloch equations provides insights into the optimum design of PARACEST agents for MRI. Magn Reson Med 2005;53:790–799. [PubMed: 15799055]
75. Zhang S, Malloy CR, Sherry AD. MRI thermometry based on PARACEST agents. J Am Chem Soc 2005;127:17572–17573. [PubMed: 16351064]
76. Muller RN, Vander Elst L, Laurent S. Spin transition molecular materials: intelligent contrast agents for magnetic resonance imaging. J Am Chem Soc 2003;125:8405–8407. [PubMed: 12837114]
77. Settecase F, Sussman M, Roberts T. A new temperature-sensitive contrast mechanism for MRI: Curie temperature transition-based imaging. Contrast Media Mol Imaging 2007;2:50–54. [PubMed: 17304641]

78. Germain D, Chevallier P, Laurent A, Savart M, Wassef M, Saint-Jalmes H. MR monitoring of laser-induced lesions of the liver in vivo in a low-field open magnet: temperature mapping and lesion size prediction. J Magn Reson Imaging 2001;13:42–49. [PubMed: 11169802]

79. Germain D, Vahala E, Ehnholm GJ, Vaara T, Ylihautala M, Savart M, Laurent A, Tanttu J, Saint-Jalmes H. MR temperature measurement in liver tissue at 0.23 T with a steady-state free precession sequence. Magn Reson Med 2002;47:940–947. [PubMed: 11979573]

80. Bohris C, Schreiber WG, Jenne J, Simiantonakis I, Rastert R, Zabel HJ, Huber P, Bader R, Brix G. Quantitative MR temperature monitoring of high-intensity focused ultrasound therapy. Magn Reson Imaging 1999;17:603–610. [PubMed: 10231187]

81. Rieke, V.; Butts Pauly, K. Echo combination to reduce temperature measurement errors in the presence of fat. Proceedings 24th Annual Meeting ISMRM; Seattle, WA. 2006.

82. McDannold N, Hynynen K, Jolesz F. MRI monitoring of the thermal ablation of tissue: effects of long exposure times. J Magn Reson Imaging 2001;13:421–427. [PubMed: 11241817]

83. Stafford RJ, Price RE, Diederich CJ, Kangasniemi M, Olsson LE, Hazle JD. Interleaved echo-planar imaging for fast multiplanar magnetic resonance temperature imaging of ultrasound thermal ablation therapy. J Magn Reson Imaging 2004;20:706–714. [PubMed: 15390144]

84. Weidensteiner C, Kerioui N, Quesson B, de Senneville BD, Trillaud H, Moonen CTW. Stability of real-time MR temperature mapping in healthy and diseased human liver. J Magn Reson Imaging 2004;19:438–446. [PubMed: 15065167]

85. Guo JY, Kholmovski EG, Zhang L, Jeong EK, Parker DL. k-space inherited parallel acquisition (KIPA): application on dynamic magnetic resonance imaging thermometry. Magn Reson Imaging 2006;24:903–915. [PubMed: 16916708]

86. Bankson JA, Stafford RJ, Hazle JD. Partially parallel imaging with phase-sensitive data: Increased temporal resolution for magnetic resonance temperature imaging. Magn Reson Med 2005;53:658–665. [PubMed: 15723414]

87. de Zwart JA, Vimeux FC, Palussiere J, Salomir R, Quesson B, Delalande C, Moonen CT. On-line correction and visualization of motion during MRI-controlled hyperthermia. Magn Reson Med 2001;45:128–137. [PubMed: 11146494]

88. Stafford RJ, Hazle JD, Glover GH. Monitoring of high-intensity focused ultrasound-induced temperature changes in vitro using an interleaved spiral acquisition. Magn Reson Med 2000;43:909–912. [PubMed: 10861889]

89. Scheffler K. Fast frequency mapping with balanced SSFP: theory and application to proton-resonance frequency shift thermometry. Magn Reson Med 2004;51:1205–1211. [PubMed: 15170841]

90. Paliwal V, El-Sharkawy AM, Du X, Yang X, Atalar E. SSFP-based MR thermometry. Magn Reson Med 2004;52:704–708. [PubMed: 15389940]

91. Rieke, V.; Hargreaves, B.; Butts Pauly, K. PRF shift thermometry using multiple-acquisition phase-cycled SSFP. Conf Proc 6th Interventional MRI Symposium; 2006.

92. Salomir R, de Senneville BD, Moonen CT. A fast calculation method for magnetic field inhomogeneity due to an arbitrary distribution of bulk susceptibility. Concepts in Magnetic Resonance Part B: Magnetic Resonance Engineering 2003;19B:26–34.

93. Morikawa S, Inubushi T, Kurumi Y, Naka S, Sato K, Demura K, Tani T, Haque HA. Feasibility of respiratory triggering for MR-guided microwave ablation of liver tumors under general anesthesia. Cardiovasc Intervent Radiol 2004;27:370–373. [PubMed: 15129346]

94. Lepetit-Coiffe M, Quesson B, Seror O, Dumont E, Le Bail B, Moonen CTW, Trillaud H. Real-time monitoring of radiofrequency ablation of rabbit liver by respiratory-gated quantitative temperature MRI. J Magn Reson Imaging 2006;24:152–159. [PubMed: 16767739]

95. Vigen KK, Daniel BL, Pauly JM, Butts K. Triggered, navigated, multi-baseline method for proton resonance frequency temperature mapping with respiratory motion. Magn Reson Med 2003;50:1003–1010. [PubMed: 14587011]

96. Shmatukha AV, Bakker CJG. Correction of proton resonance frequency shift temperature maps for magnetic field disturbances caused by breathing. Phys Med Biol 2006;51:4689–4705. [PubMed: 16953050]

97. de Senneville BD, Mougenot C, Moonen CTW. Real-time adaptive methods for treatment of mobile organs by MRI-controlled high-intensity focused ultrasound. Magn Reson Med 2007;57:319–330. [PubMed: 17260361]

98. Rieke V, Vigen KK, Sommer G, Daniel BL, Pauly JM, Butts K. Referenceless PRF shift thermometry. Magn Reson Med 2004;51:1223–1231. [PubMed: 15170843]

99. Kuroda K, Kokuryo D, Kumamoto E, Suzuki K, Matsuoka Y, Keserci B. Optimization of self-reference thermometry using complex field estimation. Magn Reson Med 2006;56:835–843. [PubMed: 16944467]

100. Rieke V, Kinsey AM, Ross AB, Nau WH, Diederich CJ, Sommer G, Butts Pauly K. Referenceless MR thermometry for monitoring thermal ablation in the prostate. IEEE Trans Med Imaging 2007;26:813–821. [PubMed: 17679332]

101. Shmatukha AV, Harvey PR, Bakker CJG. Correction of proton resonance frequency shift temperature maps for magnetic field disturbances using fat signal. J Magn Reson Imaging 2007;25:579–587. [PubMed: 17335067]

102. Keserci BM, Kokuryo D, Suzuki K, Kumamoto E, Okada A, Khankan AA, Kuroda K. Near-real-time feedback control system for liver thermal ablations based on self-referenced temperature imaging. Eur J Radiol 2006;59:175–182. [PubMed: 16713695]

103. Wlodarczyk W, Boroschewski R, Hentschel M, Wust P, Monich G, Felix R. Three-dimensional monitoring of small temperature changes for therapeutic hyperthermia using MR. J Magn Reson Imaging 1998;8:165–174. [PubMed: 9500276]

104. Wlodarczyk W, Hentschel M, Wust P, Noeske R, Hosten N, Rinneberg H, Felix R. Comparison of four magnetic resonance methods for mapping small temperature changes. Phys Med Biol 1999;44:607–624. [PubMed: 10070804]

105. Le Y, Glaser K, Rouviere O, Ehman R, Felmlee JP. Feasibility of simultaneous temperature and tissue stiffness detection by MRE. Magn Reson Med 2006;55:700–705. [PubMed: 16463357]

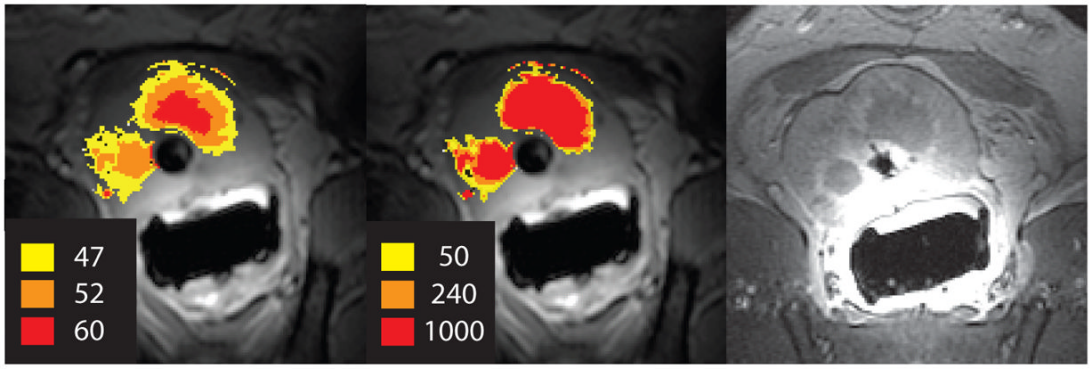

Figure 1.
Maximum temperature (left) and thermal dose map (middle) from temperature measurements during in vivo canine prostate ablation with transurethral ultrasound show good agreement with the post-treatment contrast-enhanced image (right).

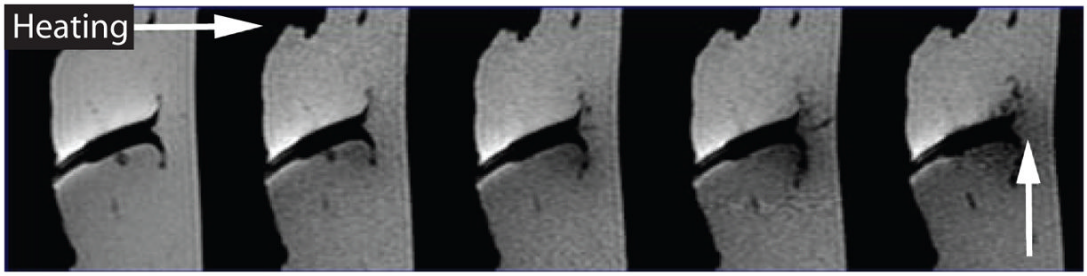

Figure 2.
T1-weighted gradient echo images acquired during RF-ablation of an ex vivo tissue sample, showing signal decrease in the heated region.

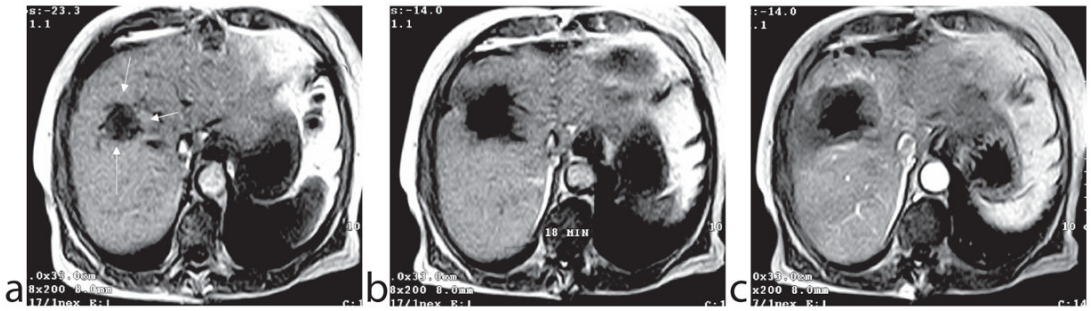

Figure 3.

Patient with relapse metastasis from a colorectal carcinoma. The T_1-weighted thermosensitive gradient echo sequence (TR/TE/flip angle: 102/8 ms/15) shows the metastasis before starting the laser ablation (a). The same imaging sequence in an advanced phase (18^{th} minute) of the intervention shows a clear drop in signal intensity in the heated area (b). The contrast enhanced T_1-weighted spin echo sequence (c) shows the immediate expansion of the necrosis and documents the complete ablation of the tumor tissue. (From: Vogl TJ, Straub R, Zangos S, Mack MG, Eichler K. MR-guided laser-induced thermotherapy (LITT) of liver tumors: experimental and clinical data. Int J Hyperthermia 2004;20:713–724. Reprinted with permission.)

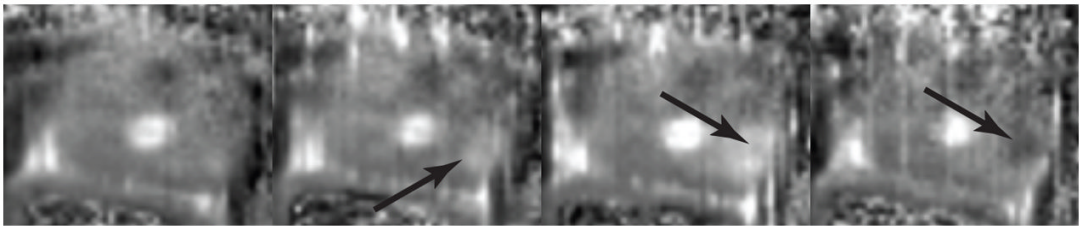

Figure 4.
Line scan ADC trace maps of the canine prostate during thermal ablation with a transurethral ultrasound applicator. Image (a) shows the ADC trace map before heating started. During heating (b), diffusion increases (arrow) due to increasing temperature. When tissue coagulation occurs, diffusion decreases although the temperature is still high (c); the arrow shows the dip inside the heating zone. After cooling back to body temperature (d), diffusion in the coagulated region remains low (arrow).

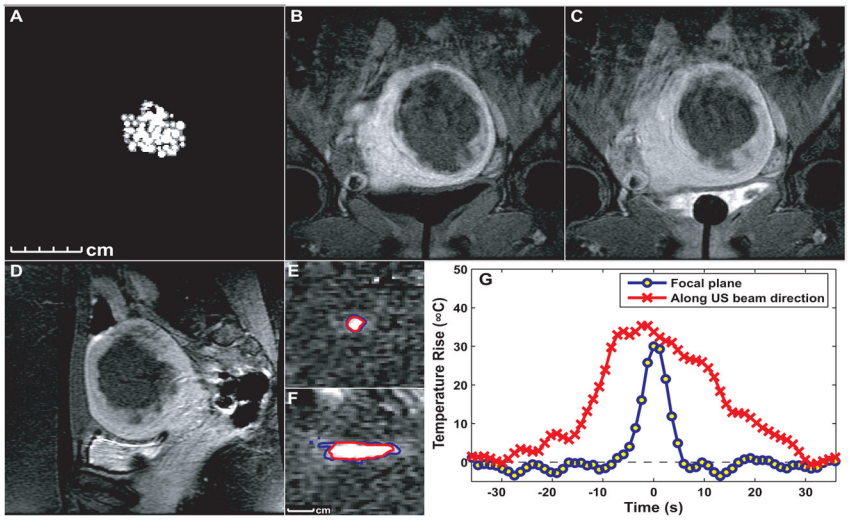

Figure 5.

Images and temperature measurement during MRI-guided focused ultrasound thermal ablation of a uterine fibroid. A: Thermal dose maps estimated from the MR thermometry acquired during treatment. Thresholds of 18 and 240 equivalent min at 43°C are shown. B–C: Coronal post-treatment contrast-enhanced T1-weighted MR images in the focal plane acquired immediately after contrast injection (B) and five min later (C). The affected fibroid tissue and non-perfused volume are larger than would be expected from the thermal measurements, presumably due to vessel occlusion during the treatment. D: Sagittal contrast-enhanced T1-weighted image (along the direction of the ultrasound beam). E–F: Thermal images acquired during two sonications in this fibroid with imaging oriented in the focal plane (E) and along the ultrasound beam direction (F). Based on the thermal dose, the lesion volume for these 20s sonication was approximately 0.7 cm^3 G: Temperature distribution through the focus at peak temperature rise for the two sonications in E–F. (images courtesy by Nathan McDannold)

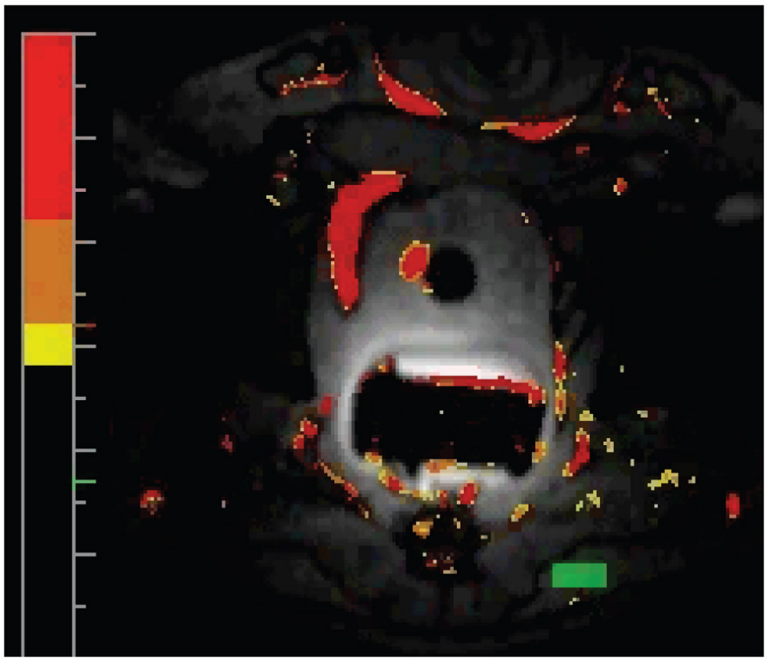

Figure 6.
Temperature measurements during in vivo canine prostate ablation. The image was acquired after the thermal treatment ended and the temperature in the prostate returned to body temperature. Thus, the apparent heating areas are caused by tissue motion and resulting misregistration between the image and its baseline.

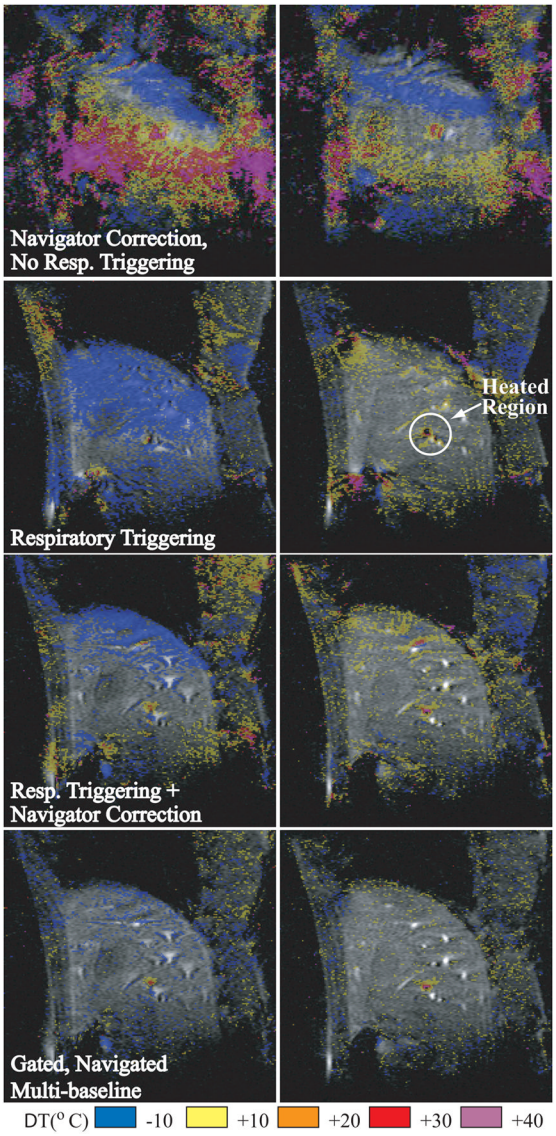

Figure 7.

Two time frames during laser heating in the liver of a pig under variable respiratory motion. Reconstructions were performed without trigger (top row), with simple respiratory triggering only (second row), respiratory triggering with navigator phase correction (third row), and the triggered, navigated, multi-baseline method (bottom row). (From Vigen KK, Daniel BL, Pauly JM, Butts K. Triggered, navigated, multi-baseline method for proton resonance frequency temperature mapping with respiratory motion. Magn Reson Med 2003;50:1003–10. Reprinted with permission.)

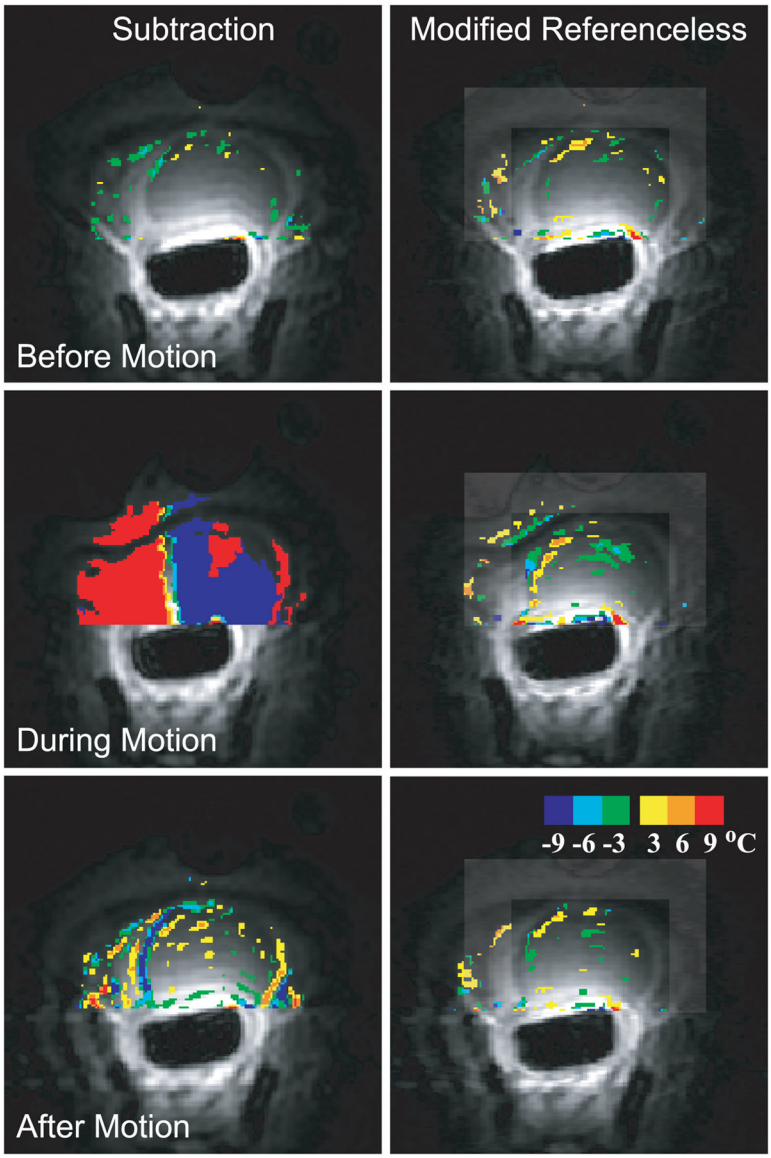

Figure 8.
Temperature images acquired in the canine prostate without application of heat comparing referenceless thermometry and baseline subtraction. Before motion, the temperature maps are similar (upper row). When tissue motion occurs (middle row), severe errors render baseline subtraction useless. After motion (bottom row), small artifacts remain with baseline subtraction but are nor as prevalent in the referenceless method. (From Rieke V, Kinsey AM, Ross AB, Nau WH, Diederich CJ, Sommer G, Butts Pauly K. Referenceless MR thermometry for monitoring thermal ablation in the prostate. IEEE Trans Med Imaging 2007;26:813–821. Reprinted with permission.)